Calibration of the axial stiffness of a single-beam acoustic tweezers

Sarah Vincent, Pascal Challande, Régis Marchiano

Calibration of the axial stiffness of a single-beam acoustic tweezers

Sarah Vincent[1,2], Pascal Challande[1], and Régis Marchiano[1]

[1]Sorbonne Université, CNRS UMR 7190, Institut Jean le Rond d'Alembert, Paris, 75005, France
[2]Sorbonne Université, CNRS UMR 7588, Institut des Nanosciences de Paris, Paris, 75005, France
[*]regis.marchiano@sorbonne-universite.fr
[+]these authors contributed equally to this work

ABSTRACT

Single-beam acoustic tweezers have recently been demonstrated capable of selective three-dimensional trapping. This new contactless manipulation modality has great potential for many scientific applications. Its development as a scientific tool requires the precise calibration of its radiation force, specifically its axial component. The lack of calibration for this force is mainly due to its weak magnitude compared to competing effects like weight. We investigate an experimental method for the calibration of the axial stiffness of the radiation force by observing the axial oscillations of a trapped bead in a microgravity environment. The stiffness exhibits a linear relationship with the acoustic intensity and is of the mN/m order. Then, a predictive model, loaded with the experimental acoustic field, is compared to the measured stiffness with very good agreement, within a single amplitude coefficient. This study paves the way to the development of calibrated acoustic tweezers.

Introduction

Contactless manipulation is the manipulation of an object without physical contact by the action of remote forces. Acoustic manipulation, based on radiation pressure like optical tweezers[1], has the advantage of being applicable to many materials regardless of their electromagnetic properties, in gases or liquids, through various acoustic emission methods. Moreover, ultrasounds have been long used for medical purposes thanks to their good compatibility with the living. The interaction of an acoustic field with an object produces the action of radiation forces on the object, induced by the variation of pseudo-momentum when the field is scattered by the object.

The first experimental demonstrations of acoustic levitation were carried out using standing waves generated by a powerful acoustic source and a reflector. The trapped objects, of the order of a few millimeters, were lead or glass balls. Standing waves still remain the most common means of acoustic manipulation. However, other types of beam, such as travelling waves[2–4] or surface waves[5] also allow for the contactless manipulation of objects. The forces generated by these different techniques can range from picoNewtons to milliNewtons (particularly for standing wave systems), and the sizes of objects manipulated range from micrometers to centimeters. Acoustic manipulation has many applications, notably in materials science[6,7], in chemistry[8], for the study of drops[9,10] and bubbles[11,12], in microfluidics[13] and in microrobotics[14]. Recent studies demonstrated the existence of a new modality for acoustic contactless manipulation: single beam acoustic tweezers[2,4], going beyond traditional standing waves and opening new perspectives especially for selective dexterous manipulation. This technology relies on acoustic focused vortex beams. Early theoretical analysis on vortex beams[15,16] and radiation forces and torque[17,18] have driven an increasing interest for this kind of beams. Their main characteristic is a helical structure with a phase singularity along the propagation axis, inducing a pressure node. As a consequence, the field intensity is low around the object, trapped on the axis, as opposed to optical tweezers. Furthermore, the magnitude of the force per surface unit is known to be proportional to the wave field intensity divided by the waves celerity in the medium ($F \approx I/c_0$). So for the same force magnitude, the acoustic intensity is drastically reduced compared to its optical counterpart. Acoustic tweezers have demonstrated selective, three-dimensional trapping capabilities, using single-sided ultrasonic beams allowing easy access to the trapped object in water[4] or air[2] thanks to good working distance and forces ranging from picoNewtons to microNewtons. The wide range of frequencies enables the manipulation of nanometers to millimeters size particles.

The development of acoustic tweezers as a scientific instrument requires a precise characterization of the radiation force. This is usually done by indirect methods, as the radiation force is intrinsically dependent on the object on which it is exerted. The balance between the buoyancy and the radiation force exerted on bubbles of radius 25 to 500 μm and generated by a focused vortex operating at 2.25 MHz has allowed the axial pushing force to be calibrated[19]. It was also characterized by measuring the displacements of a spherical steel diffuser of diameter 1.8 mm suspended by wires and subjected to the radiation force emitted by a transducer transmitting at 1.19 MHz[20]. The lateral forces, at a frequency of 1.5 MHz, exerted on beads of diameter

2 to 8 mm resting on a membrane in water, were determined by the balance of opposing lateral forces, notably the weight[21]. Other strategies for characterizing the lateral forces of radiation are based on the drag force induced in a microchannel or on the friction forces caused by the lateral displacement of objects trapped on a surface. Thus, it seems that the axial restoring force has not yet been characterized for the manipulation of spherical elastic balls, despite its importance for selective, three-dimensional and precise non-contact manipulation activities. To fill this gap, we propose to characterize experimentally the axial trap stiffness of the acoustic tweezers and to validate a three-dimensional model for the radiation force[22,23].

The radiation force is a tenuous phenomenon, often dominated by other effects. The axial restoring force is even more so sensitive to it as it is generally an order of magnitude smaller than the lateral forces, due to the progressive aspect of the field along the propagation axis and stationary along the transverse axes. In air, the radiation force is particularly challenged by the weight of the objects to be manipulated, whose densities are in high contrast to that of the medium. Despite these difficulties, the possibility of manipulating objects in air using acoustic fields has been demonstrated, in terrestrial gravity, on several occasions with standing wave systems[24–26], or with levitation systems[2]. However, either the material variety of the objects that can be manipulated is restricted (by their density) or the manipulation operations are limited due to multiple equilibrium positions (lack of preciseness) or by the size of the system (lack of accessibility). One way to get rid of the weight of the objects, for the characterization of the acoustic trap, is to realize contactless manipulation experiments in microgravity, so the weight is not a limiting factor anymore. The first experiments of acoustic levitation in space, more specifically in the laboratory of the Space Shuttle Challenger in 1985, consisted in positioning and maintaining samples in place in order to study them. One of them aimed at studying the forced rotations of a drop trapped by three orthogonal standing wave beams. Another experiment aimed at positioning glass samples, using a standing wave device (composed of an acoustic source and a reflector) operating at 15 kHz, to study their fusion[27]. Following this work, other similar experiments were carried out in a microgravity environment[28,29]. More recently, drop manipulation, coalescence, mixing, separation, and evaporation have been achieved using a transducers array and reflector[10]. The simultaneous manipulation of two droplets of diameter about 4 mm is demonstrated. The use of such devices in microgravity has the advantage of not requiring too high acoustic amplitudes, which could lead to non-linear propagation effects or surface instabilities of the molten drops or samples.

In this work, we propose to perform manipulation experiments in microgravity to show 1) the possibility to trap heavy beads made of various materials, 2) to experimentally calibrate the axial stiffness observing the dynamics of the beads as proposed by[30] and 3) to validate a recent theoretical model of single-beam acoustic tweezers. The paper is organize as follow. In the first section, the different methods are explained: we start with a general description of the experiment in microgravity, then we present the single-beam acoustic tweezers, the characterisation of its radiated ultrasonic field and we conclude this section by recalling the main theoretical results about the axial stiffness produced by the acoustic tweezers. The second section contains the results and subsequent discussions. This section starts with the observations of stable traps. Then, the dynamic of the beads is used to calibrate the axial stifness, finally the measured stiffness is compared to the one predicted the theoretical 3D model.

Methods

Microgravity experiments

Microgravity is generated by parabolic flights (operated by Novespace company). In steady flight, the vertical component of the acceleration due to gravity is approximatively 1g (the same as on the ground). To generate the microgravity phases, the aircraft performs a parabola which generates 3 distinct phases: 1) a first phase lasting approximately 30 s where the vertical component of gravity increases to 1.8g, 2) a microgravity phase for a duration of 22 s, the acceleration due to gravity is then of the order of around ± 0.05g and 3) a new phase of 30 s at 1.8g. This maneuver is repeated several times to iterate the experiments. In the cabin aircraft, ambient temperature is between 17 and 20°C, the pressure is set to 825 ± 5 hPa. As a result, the air density is slightly lower than that on the ground and equal to 0.985 kg/m^3, according to the ideal gas law. The decrease of air density induces the strengthening of the radiation force (cf. Equation 3). Sound wave velocity is not affected and is 342 m/s.

The experimental procedure for contactless manipulation consists in depositing a bead of expanded polystyrene (EPS) of diameter between 2 and 4 mm in the acoustic trap, maintained during the whole parabola and serving as a visual target to inject the bead of interest during the microgravity phase. Once the latter is trapped, the EPS bead is meticulously removed from the trapping area, trying to disturb the stability of the trap as little as possible. When the trapped object undergoes external disturbances, from gravity variations or from the initial conditions set by the withdrawal of the trap from the EPS bead, it oscillates. These oscillations, recorded by cameras can be related to the trap stiffness. To achieve a complete calibration, the oscillations are observed for several objects referenced in Table 1 and acoustic pressure amplitudes, as the radiation force and its stiffness depend on the pressure amplitude, the size of the object and its mechanical properties.

The experimental setup is shown in Figure 1. It consists of an single-beam acoustic tweezers fixed inside a glove box. The experiments are carried out within the airplane's cabin where other experiments are located. It is therefore important to ensure that all used objects do not roam around the rest of the cabin. This explains the use of the glove box which is not necessary for the use of the acoustic tweezers in other cases. Note that the upper part of the glove box is lined with an acoustic absorber to

Materials	Density (kg/m^3)	Young's modulus (GPa)	Poisson's ratio	Diameter (mm)
Polypropylene (PP)	870	1.285	0.43	2.381 and 4.762
Polyamide (PA)	1110	2.5	0.4	2.381 and 4.762
Polyacetal (POM)	1379	64	0.44	2.381 and 4.762
Borosilicate glass (BG)	2230	64	0.2	2 and 4.762
Al_2O_3 Ceramic (AOC)	3850	400	0.22	2.381

Table 1. Beads' materials, mechanical properties and diameters.

prevent the appearance of standing waves in the device The side walls have no impact on the sound field, as they are far enough away, moreover the sound field is highly directional and focused, thus very localized in space. There are three cameras: the two side-cameras, recording in the (xz) and (yz) axial planes, are IDS UI-3080CP-M-GL Rev.2 (AB00848) with a 50 Hz frame rate, equipped with Fujifilm CF-ZA-1S lenses, the third camera on the top is a GoPro (not used in this paper). Figure 1 shows only the upper stage of the rack fixed in the aircraft cabin and used during the experiments. The lower stage (not shown here) is used to attach an accelerometer and the acoustic tweezers control electronics.

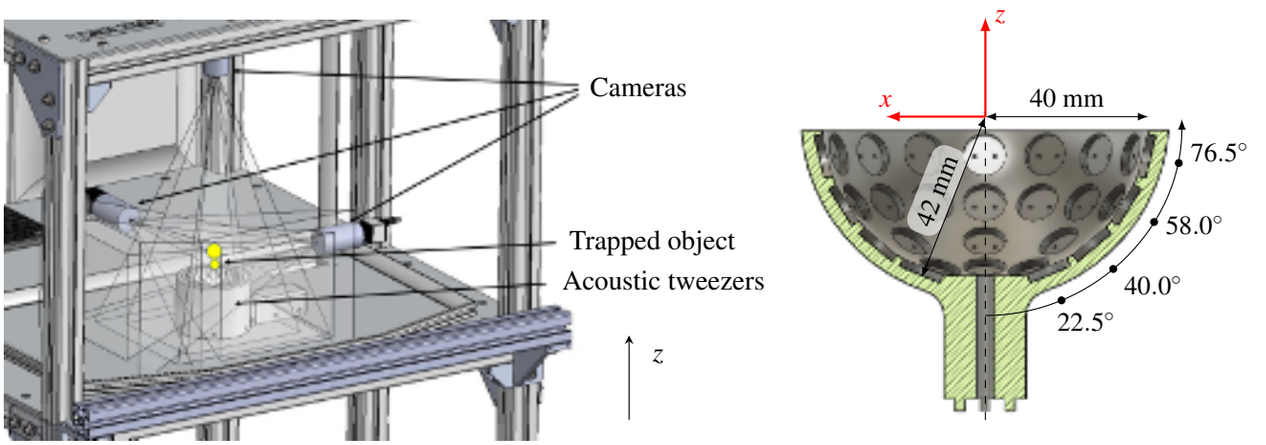

Figure 1. (Left) Experimental setup - The acoustic tweezers, attached to the upper stage of the rack, is facing upwards such that its propagation axis z is opposed to the ground gravity. The spherical particles are carefully deposited in the acoustic trap. The cameras (only 2 of the 3 are used) are filming the trapping. An accelerometer (in the lower stage of the rack not appearing in the figure) is measuring the gravity variations in the cabin. (Right) Cut view of the acoustic tweezers and geometrical disposition of the transducers (only the transducers'prints are shown).

Single-beam acoustic tweezers

Inspired by previous works[3,4], we built a single-beam acoustic tweezers consisting of 48 Murata MA40S4S piezoelectric ultrasonic transducers (10 mm diameter, operating in air at a frequency $f_0 = 40$ kHz), distributed over a portion of sphere of resulting internal radius 3.3 cm in 16 columns (separated by an azimutal angle of 22.5°), alternating between 2 or 4 ranks of transducers (located at elevation angles $22.5, 40, 58$ and $76.5°$ from the bottom) (cf. Figure 1 - right). In practice, the transducers are mounted in a hemi-spherical resin dome made with a 3D printer. The signals emitted by the transducers are generated by control electronics with 16 independent channels (one channel per column, supplied by an amplifier capable to deliver up to 20 V_{pp}. All operations are controlled by a FPGA (Intel Cyclone 10LP)). The spherical shape and the independent actuation of each of the 16 channels allow the generation of a naturally focused vortex beam of topological charge m', with a phase singularity and pressure node on the axis of propagation. The topological charge defines the number of phase jump the wavefront will experience in the same plane. Throughout the calibration of the axial force, m' will be set to ± 1.

The incident acoustic pressure field is measured at the focal plane, using a 1/8" Gras 46DE microphone. We use the calibration provided by the manufacturer indicating a ± 3 dB uncertainty. Beforehand, we checked that the microphone properly recovered the sound pressure level of a calibrated pistonphone operating at 250Hz. To realize the pressure field measurement, 40 kHz sinusoidal signals are transmitted to the transducers for a duration of 255 periods, ensuring that each emitted wave can properly interfere with each other in the focal plane, where the field is measured. At each spatial coordinate of the plane of dimensions 60 mm $\times$ 60 mm, sampled in 3721 points, the time-varying pressure field is measured using a synchronized trig, so

the phase of the vortex is well recovered. Then, the 40 kHz operating frequency is selected in the spectrum of each signal, to switch in the harmonic regime. The resulting measured field $\hat{p}_{m'=1}(x,y,f_0)$ is shown Figure 2.

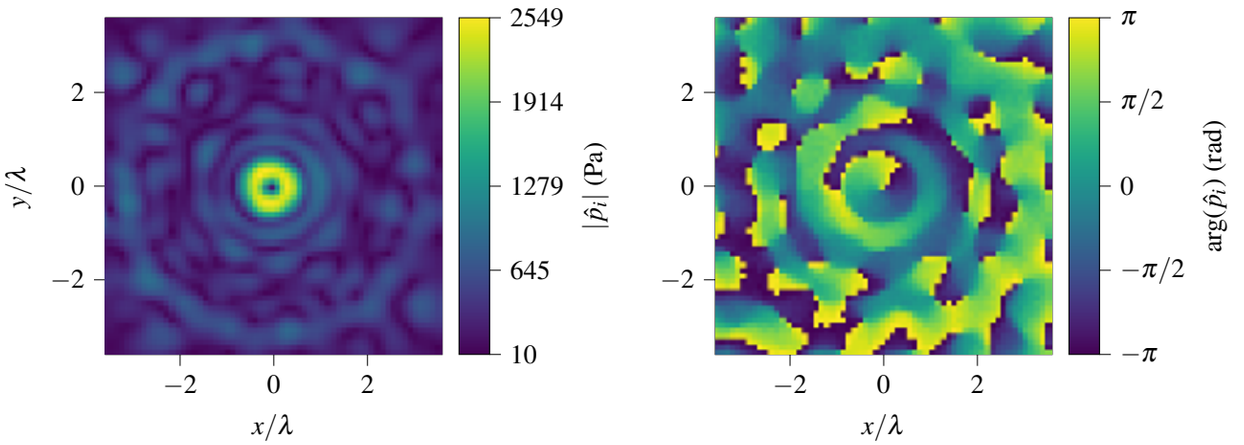

Figure 2. Acoustic incident pressure field measured in the focal plane $z = 0$ of the vortex field of topological charge 1 : modulus (left) and phase (right). The pressure amplitude is obtained by supplying the transducers a reference peak voltage V_p^{ref} of 5.3 V.

The phase field displays the typical helicoidal structure with a straight jump phase of 2π inside the pressure ring of radius $\lambda/2$, where the field amplitude is maximal. At the center, the phase is undefined and the modulus of the field cancels out. Outside of the pressure ring, the amplitude is much weaker and the field shows some kind of secondary rings. In theory these secondary lobes are perfectly circular. In practice, due to the discretization of the emission surface, geometric uncertainties introduced during the assembly of the transducers and/or alignment errors in the measurement, these secondary lobes are disturbed. However, their structure does not really affect the radiation force, which is of interest inside the ring. Therefore, the vortex beam is correctly synthesized. After the determination of the beam shape coefficients of the incident field, using the Angular Spectrum Method[23,31], the radiation force can be estimated. As can be seen Figure 4, the field synthesis allows the generation of a three-dimensional trapping force including an axial restoring force (cf. following section).

Acoustic vortices can induce the rotation of the object if it is absorbing the acoustic energy[32]. Baresch[33] showed that the rotation can be tuned as desired, and does not destabilize the trap in water. However, in air, Marzo[3] showed the necessity to neutralize the rotation to ensure stable trapping. To this end, the acoustic field is alternating between vortices of topological charge $m' = 1$ and $m' = -1$ on a empirically chosen switching rate of 8 periods. The acoustic period $T = 1/f_0$ is 25 μs. This duration is much shorter than the characteristic time of rotation of a sphere[34]:

$$\tau = \frac{J}{\tilde{D}} = \frac{\frac{2}{5}ma_p^2}{8\pi\mu a_p^3} = \frac{1}{15\mu}\rho_p a_p^2,$$

where J is the moment of inertia, $\tilde{D}$ the angular drag coefficient of the sphere, m its mass, ρ_p its density, a_p its radius and μ the medium dynamic viscosity. In the case of an Polypropylene bead of diameter 2 mm, $\tau \approx 3$ s. The duration of the emission of a vortex, 8 periods, is thus much lower than the characteristic time of rotation.
To realize this alternation, the sinusoidal signal is made of 8 periods of sinusoid with specific phase depending on the channel position, then of the same signal read backwards. This cycle is repeated on the whole emission duration. Depending on the emission channel, the transition from on signal sequence to another is either very accentuated, invisible or in between. This results in the modulation of the wave field and in the diminution of the pressure amplitude at some positions in the field. The transducers being very resonant at the working frequency, their response is quite slow to fast switching and cannot manage to reach a permanent emission regime, inducing a loss of emitted acoustic energy. The pressure signals for a single vortex beam $m' = 1$ and for a modulated field $m' = +1, -1$ can be seen Figure 3, measured at the same coordinate on the pressure ring of the vortex, in the focal plane.

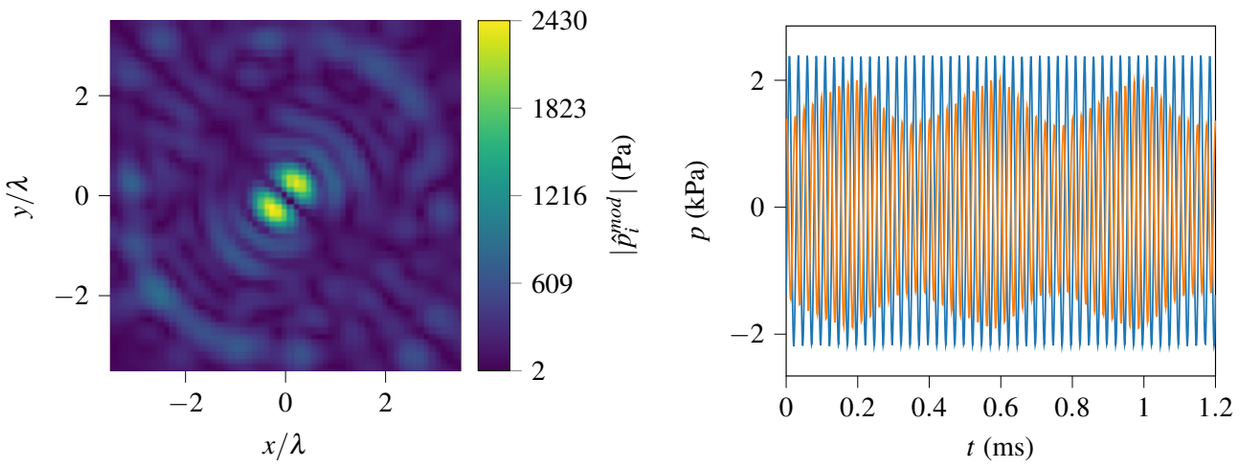

Figure 3. (Left) Amplitude of the incident modulated field measured in the same focal plane as Figure 2. (Right) Comparison of the pressure signals measured at the same coordinate ($y = 2$ mm $= 0.23\lambda$, $x = 0$) in the focal plane $z = 0$ in terms of time, when the field is a unique focused vortex of topological charge 1 (blue) and when it is periodically alternating between two vortices of charge 1 and -1 (orange).

Theoretical model

Acoustic tweezers rely on acoustic radiation force, which is a mean force exerted by the acoustic pressure field $p(\vec{x},t)$ on the surface of an object and takes the general expression:

$$\vec{F} = \left\langle \int_{S(t)} p(\vec{x},t) d\vec{S} \right\rangle. \tag{1}$$

The acoustic pressure field results of the superposition of the incident field and a scattered field by the object :

$$p(\vec{x},t) = p_i(\vec{x},t) + p_s(\vec{x},t) \tag{2}$$

Assuming an arbitrary harmonic wave field and a spherical elastic bead in a perfect fluid, the acoustic radiation force can be expressed analytically[35]. As this paper focuses on the calibration of the axial radiation restoring force, only the axial component F_z of the three-dimensional force is recalled[31]:

$$F_z = -\frac{p_0^2}{2\rho_0\omega_0^2} \sum_{n=0}^{\infty} \sum_{m=-n}^{m=n} Im\left\{ G_n^m A_n^{m*} A_{n+1}^m C_n \right\}, \tag{3}$$

where p_0 is a characteristic pressure of the incident harmonic pressure field $p_i(\vec{x},t) = \hat{p}_i(\vec{x})e^{-i\omega_0 t}$, ρ_0 is the density of the fluid and ω_0 is the angular frequency. The coefficients G_n^m depend on the integers n and m (respectively the radial degree and the azimuthal order), $G_n^m = \sqrt{(n+m+1)(n-m+1)}/\sqrt{(2n+1)(2n+3)}$ and the coefficients $C_n = R_n^* + R_{n+1} + 2R_n^* R_{n+1}$ are linked to the scattering coefficients R_n whose values depend on the bead size and mechanical properties. The coefficients A_n^m are the beam shape coefficients coming from the spherical harmonics decomposition of the incident pressure field $\hat{p}_i$:

$$\hat{p}_i(r,\theta,\varphi) = p_0 \sum_{n=0}^{\infty} \sum_{m=-n}^{m=n} A_n^m j_n(kr) Y_n^m(\theta,\varphi), \tag{4}$$

with $j_n(kr)$ is the spherical Bessel function, $k = \omega_0/c_0$ the wave number, and $Y_n^m(\theta,\varphi)$ are the spherical harmonics. The scattered pressure by the sphere is:

$$\hat{p}_s(r,\theta,\varphi) = p_0 \sum_{n=0}^{\infty} \sum_{m=-n}^{m=n} R_n A_n^m j_n(kr) Y_n^m(\theta,\varphi). \tag{5}$$

The spherical coordinates (r,θ,φ) are expressed in terms of the cartesian coordinates (x,y,z) as $r = \sqrt{x^2+y^2+z^2}$, $\theta = \arccos(z/r) \in [0,\pi]$ and $\varphi = \arctan(y/x) \in [0,2\pi]$.

The beam shape coefficients can be recovered from the measurements of the pressure field in the focal plane[23,31]. The axial restoring force produced by a vortex beam on a polypropylene spherical particle of diameter 4.762 mm is shown in Figure 4. The origin of the axis represents the focal point of the field. It appears that the axial force exhibits a positive part, pushing away the particle, and a negative part, pulling it towards the focus, where the particle will be stably trapped. Around the stable position, the force is directly proportional to the distance from the equilibrium position. Thus, the approximation $F_z \approx -k_z z$, with k_z the stiffness of the trap, seems reasonable in this region.

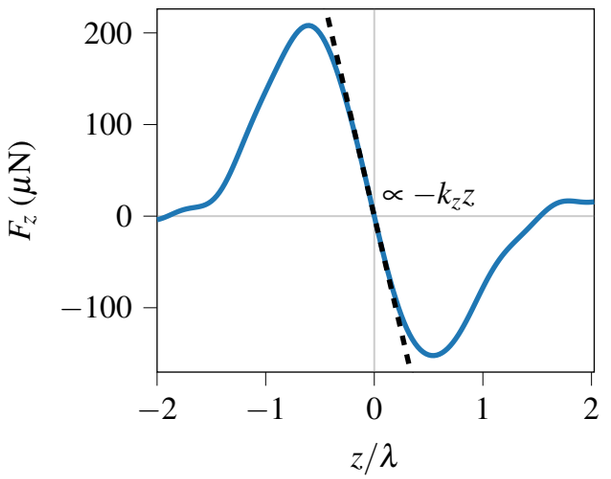

Figure 4. Theoretical axial restoring force for a polypropylene bead of diameter 4.762 mm. The z-axis is centered on the focus of the beam, and expressed in terms of the wavelength $\lambda = c_0/f_0 = 8.5$ mm. The dashed line is the linear approximation of the axial force around the equilibrium position, its slope corresponds to the local stiffness of the trap, which is about 60 mN/m.

Results and Discussion

Trapping observations

As can be seen in Figure 5, all the beads tested were successfully trapped during the 22 seconds microgravity experiments. These stable trappings validate the generation of three-dimensional trapping forces by the 40 kHz acoustic tweezers. Indeed, in microgravity, it is no longer possible to obtain the stability of the object by counteracting the weight, it is necessary to maintain it in a fixed position while applying forces directed towards this position. The bead's position in the trap depends mainly on the size of the object and its residual weight in microgravity. The trap is relatively stiff, which allows the bead to oscillate when triggered by external perturbation, such as gravity variations in the aircraft cabin or initial conditions. So, in addition, the bead's position will also depend on its dynamical movement in the trap. The trapping of the larger, and thus heavier beads tends to be less stable. Therefore, some observations are of short duration because of the ejection of the trapped object. This ejection can be fast or slow, during the stall of the bead at the extremity of an oscillation.

Calibration of the axial restoring force

The beads' oscillations are mainly driven by the vertical acceleration variations in the aircraft cabin and the initial conditions set at the bead injection. The oscillations are then recovered by a standard tracking algorithm and are synchronized to the vertical acceleration measured next to the tweezers and the acoustic voltage of emission. Those data are shown in Figure 6 for a 2.381 mm diameter Polypropylene bead and for a 4.762 mm diameter Polyamide bead (see Table 1 for mechanical properties). It clearly appears that the vertical acceleration steers the oscillation envelope. The axial radiation force and the trapped object act like a spring-mass system, where the oscillations angular frequency ω_B of the bead is related to the stiffness k_z by:

$$\omega_B = \sqrt{k_z/m}, \tag{6}$$

with m the mass of the object. Moreover, around the equilibrium position (cf. Figure 4), the force is linear and proportional to $k_z z$, which will also be proportional to the square of the pressure amplitude (Equation 3). Hence, the oscillations angular frequencies are computed for several objects, as well as for several acoustic emission levels that will be expressed as the peak voltage V_p transmitted to the transducers. The angular frequencies ω_B are recovered from the oscillations spectrum and plotted

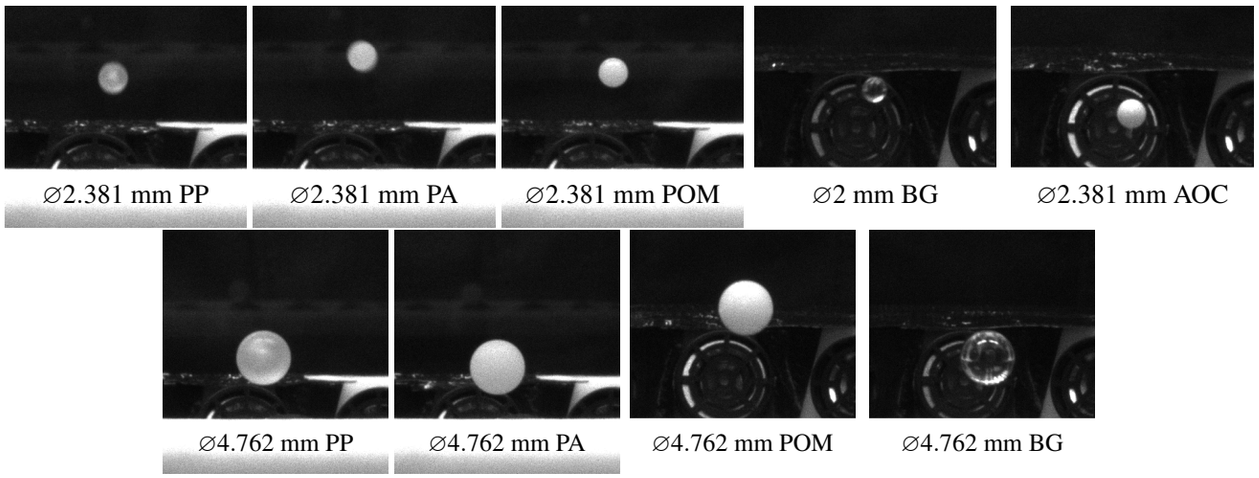

Figure 5. Stable trapping observations of several beads (listed in Table 1) under microgravity conditions by the acoustic tweezers. The images are captured by the camera on behind the acoustic tweezers in Fig. 1 (left).

for each bead in terms of V_p in Figure 7 (points with error bars). The error bars are related to the duration of the signal used to compute the oscillation frequency; the uncertainty is then equal to:

$$\delta\omega_B = 2\pi f_r / N_t, \tag{7}$$

with f_r the camera frame rate which is 50 Hz and N_t the number of time samples. The measurement points are restricted to a voltage range bounded by 6.2 V and 10.5 V, as the beads could not be trapped by acoustic amplitudes below this range, and the maximum voltage delivered to the transducers corresponds to the upper limit.

From Figure 7, the relation $\omega_B = \alpha V_p$ appears, with $\alpha = \alpha(a_p, \rho_p)$ a function of the radius of the particle a_p and its density ρ_p. Accordingly, $k_z = \beta(a_p, \rho_p) V_p^2$, which complies with the radiation force being proportional to the field intensity. The experimental data can be fitted by a linear regression (see dashed lines in Figure 7). This is done using the least squares method and by adding the point $(V_p = 0, \omega_B = 0)$ to the measurement series, however the linear regression is not forced to 0. The Pearson correlation coefficients obtained for each series are greater than 0.98 and thus indicate a strong linear relationship between the voltage and the beads oscillations.

A further analysis of the uncertainties on the observed oscillations, Figure 8, shows that they are higher for the biggest and heaviest beads represented by diamonds, or of green and purple color, whose oscillations are of lower frequency. Their uncertainties are above the average, and sometimes with a large shift as for the glass and ceramic beads of diameters 2 and 2.381 mm respectively. This tendency reflects the difficulty, during experiments of manipulation in microgravity, to insert these beads correctly in the trap, because of a non-zero residual gravity, resulting in shorter observations. Indeed, the weight of the beads is proportional to the radius cubed of the particles. Thus, going from a bead of 2.381 mm diameter to 4.762 mm, i.e. doubling the radius, is equivalent to multiplying the weight by a factor of 8. However, the radiation force is only multiplied by a factor of factor 2.8 for the positive peak and a factor 3.5 for the negative peak. With regard to the stiffness, which is measured from the oscillations, it is multiplied by a factor 2.8 also. Therefore, the weight, even residual, has a strong impact on the ease of trapping a bead and on its stability. Also, the weight increases with the density while the radiation force is the same for all the beads, of the same radius, used here. Indeed, the density contrast between the bead's material and air, mainly driving the force magnitude, is saturated from a value of 500. Here the lightest material, the Polypropylene, has a density greater than $800\rho_0$. Hence, the radiation force does not vary from one material to another.

The uncertainties on the angular frequency of the oscillations are on average about 11%. These values are correct compared to many other measurement sensors. On the other hand, similar experiments to characterize the radiation force[19] had experimental uncertainties between 20 and 30%.

Comparison with the 3D model for the axial component of the radiation force

In order to compare the experimental results with the three-dimensional model, the theoretical force is computed, knowing the size and properties of the object and the beam shape coefficients of the measured incident field, which is a focused vortex of topological charge $m' = 1$. The theoretical stiffness k_z^{th} corresponds to the local slope of the force, around the abscissa point corresponding to the cancellation of the axial force, which neglects the weight of the object. Since the acoustic field

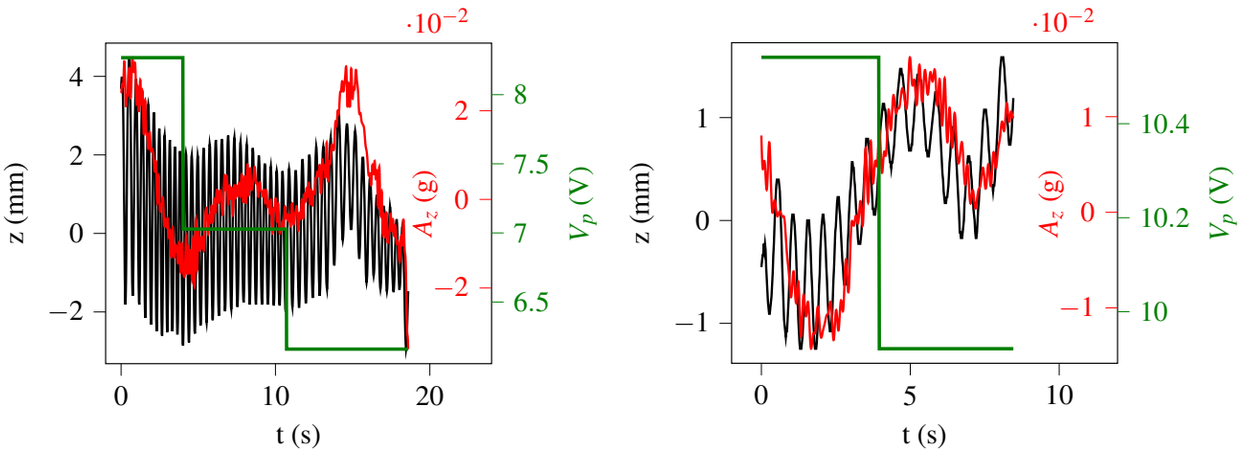

Figure 6. Axial oscillations of a 2.381 mm Polypropylene (PP) bead (left) and a 4.762 mm Polyamide (PA) bead (right) during a microgravity experiment. The vertical acceleration expressed in $g = 9.81$ m.s^{-2}, measured during the experiment, is plotted in red. The peak emission voltage, driving the acoustic pressure amplitude is plotted in green and is varying during the experiment.

was measured at a single emission amplitude, it is necessary to apply a scaling step to compute the radiation force at other amplitudes. Assuming linear acoustic propagation, the force computed from the measured field is rescaled by the coefficient $(V_p/V_p^{ref})^2$, where V_p is the peak voltage supplied to the transducers during the trapping experiments and $V_p^{ref} = 5.3$ V is the reference peak voltage corresponding to the 2D pressure field measurement used to estimate the beam shape coefficients. The maximum voltage delivered by the system is 10.5 V.
It is noted that nonlinear effects are neglected despite the high pressure amplitudes measured (cf. Figure 2). Indeed, a simple way to quantify these effects is to select the second harmonic at 80 kHz in the spectrum of the measured signals, determine its beam shape coefficients using the angular spectrum method and estimate the radiation force generated. The force has an amplitude of about 1% of that at the fundamental frequency 40 kHz. Thus, the presence of non-linear effects is neglected.

The direct comparison of the theoretical and experimental results, which is not shown here, indicates a systematic overestimation of the theoretical model by a factor of about 2. That difference is due to experimental uncertainties and to differences between the experiments and the assumptions of the theoretical model.

The main experimental uncertainties concern the calibration of the microphone. The manufacturer assumes an accuracy of ±3 dB at 40 kHz, potentially resulting in an uncertainty of a factor of $1/\sqrt{2}$ to $\sqrt{2}$ on the pressure amplitude.

There are several differences between the assumptions of the theoretical model and the experiments. First, the field actually generated in the experiments corresponds to the rapid alternation of two vortices of opposite charges contrarily to the theory which assumes a pure vortex beam. This results in the modulation of the acoustic field (cf. Figure 3) associated to a weaker amplitude for the modulated signal than the pure one. Thus, it can be assumed that the axial force generated by the modulated field is weaker than that generated by a pure vortex. Therefore, a factor on the field amplitude or on the theoretical stiffness should be able to take into account this modulation. Then, the presence of acoustic streaming, also neglected in the theory, could affect the results. The acoustic streaming is a stream flow generated by the attenuation of sound in the bulk of the fluid[36–39]. If this flow is generated by the ultrasonic tweezers, it can induce a drag force on the bead which could shift the equilibrium position of the bead and thus slightly change the stiffness value. Finally, the variation of the residual gravity in the aircraft cabin has a strong influence on the equilibrium position of the bead, which thus varies during the oscillations (cf. Figure 6). The level of residual gravity during a parabolic manoeuvre varies between -0.04g and 0.025g (between −0.023g and 0.011g on average), which can lead to a decrease in stiffness of a factor of 0.88. The last two effects vary either as a function of time (residual acceleration) or as a function of the position of the bead in the trap (acoustic streaming) and may also explain why some points do not quite line up with the linear regressions (cf. Figure 7).
The effects described above are difficult to take into account in theoretical modeling. Therefore, we propose to identify a single amplitude factor γ including all these effects allowing the theoretical stiffnesses to match the experimental ones. This coefficient is determined using the least squares method applied to the theoretical model of the radiation force (cf. Equation 3),

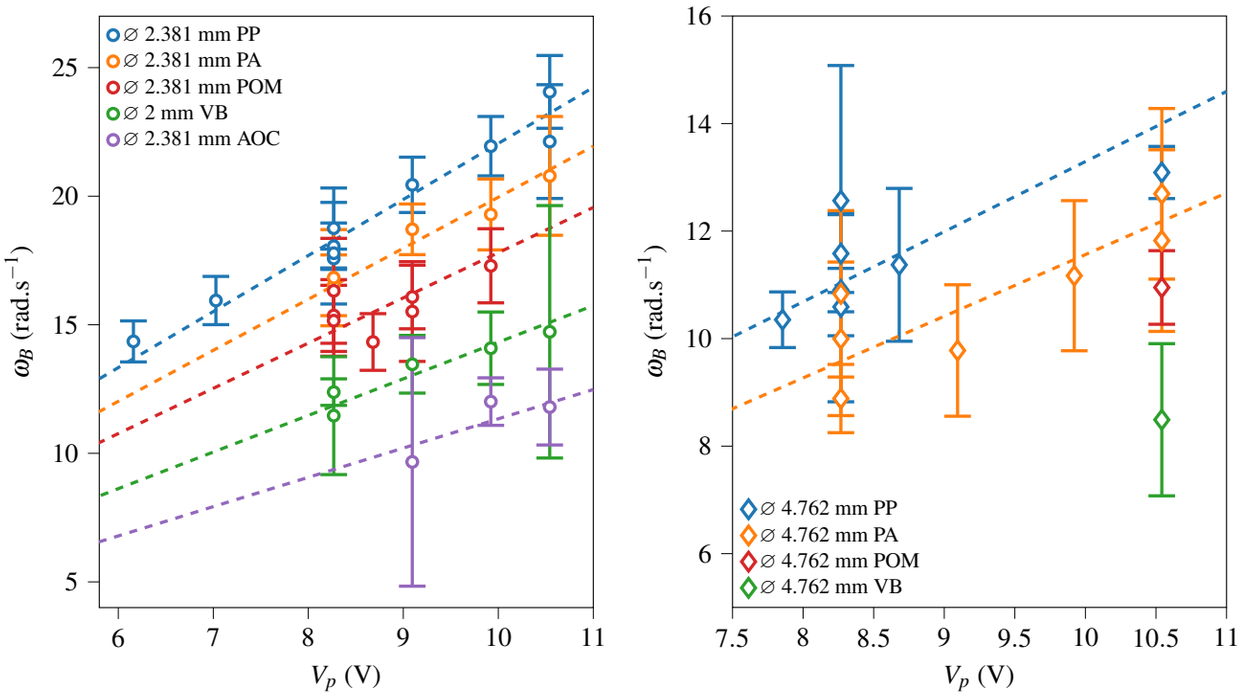

Figure 7. Experimental (points with error bars) angular frequencies ω_B for various beads (see Table 1) in terms of the acoustic amplitude, expressed as the peak voltage supplied to the transducers. Experimental error bars are defined according to the time duration of the observed oscillations used to compute the spectrum and equal to $\pm 2\pi f_r/N_t$, with $f_r = 50$ Hz the camera frame rate and N_t the number of time samples used to compute ω_B. The experimental data are fitted by a linear regression (dashed lines) with Pearson correlation coefficients greater than 0.98 (for each series).

its value is found to be about $\gamma = 0.4$ and is applied to the theoretical stiffness as:

$$k_z^{th,\gamma} = \gamma^2 k_z^{th}. \tag{8}$$

This allows to realign the theoretical stiffnesses to the experimental ones with a very good agreement, Figure 9. Each bead radius is treated separately for a better visibility of the results. The experimental stiffness is obtained by:

$$k_z = \omega_B^2 m. \tag{9}$$

The stiffnesses are approximately the same for beads with the same diameter. This was found numerically when computing the radiation force for the various beads used. Here, the differences in density between the various materials used have little impact on the radiation force and thus on the stiffness of the trap. As the experiment takes place in air, the density contrast between the medium and the particle is already very large for the lightest bead. Increasing the density does not increase the amplitude of the radiation force any further.
Thus, a single amplitude factor allows the theoretical model of the radiation force to be adjusted to the experimental results and their uncertainties.

The differences between the experimental stiffnesses and those computed with the rescaled radiation force model are expressed as:

$$\frac{\left|k_z - k_z^{th,\gamma}\right|}{k_z^{th,\gamma}} * 100\ (\%), \tag{10}$$

and are plotted Figure 9d in terms of the percentage of the experimental uncertainties, which are calculated by:

$$\delta k_z = \left|\frac{\partial k_z}{\partial \omega_B}\right| \delta\omega_B = 2m\omega_B \delta\omega_B. \tag{11}$$

The average error is about 9%, the minimum error 0.2% and the maximum error 33%. These deviations do not seem to depend specifically on the force amplitudes (related to the acoustic emission amplitudes), nor on the experimental uncertainties.

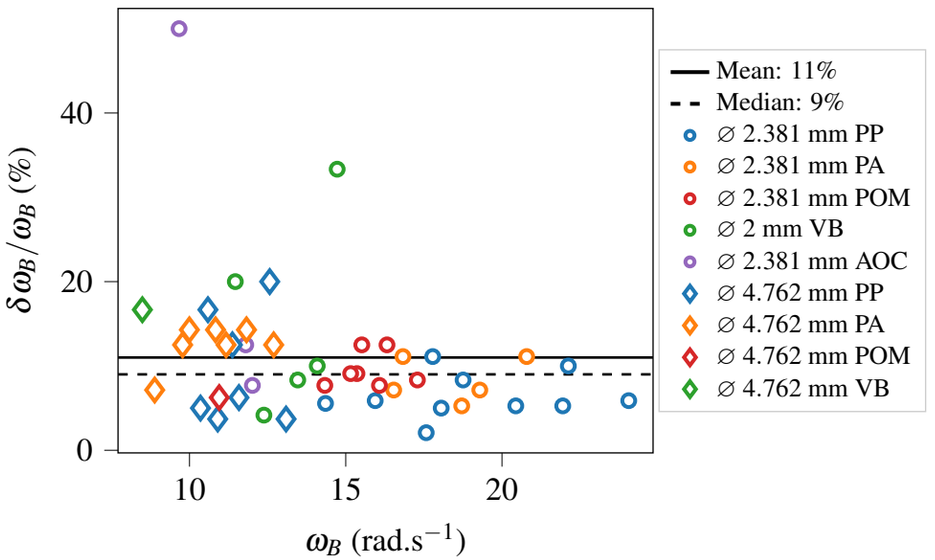

Figure 8. Experimental uncertainty of the angular frequency $\delta\omega_B$ (cf. Equation 7) for each measurement point. The uncertainty is related to the observation duration of the oscillations and is normalized by the angular frequency. Each bead is designated by a symbol and a color. The average and median of the uncertainties are respectively plotted in black solid and dashed lines.

Finally, these results indicate that the acoustic field measurement provides the theoretical force corresponding to the experimental force, within a single amplitude factor including acoustic field modulation, microphone-related uncertainty, acoustic streaming and residual gravity.

Conclusion

The work reported here focuses on the single-beam acoustic tweezers and the calibration of its axial stiffness. The acoustic device, working at a 40 kHz frequency in air, allows for the selective three-dimensional trapping of heavy spherical objects of diameter 2, 2.381 and 4.762 mm thanks to the synthesis of a progressive focused vortex beam. Trapping experiments are observed in a microgravity environment, reducing the weight of the beads to a minimum. The analysis of several beads' dynamics leads to the experimental calibration of the trap stiffness in terms of the beads' material properties and the acoustic amplitude. It is found that the trap stiffness reaches a maximum value of 10 mN/m for the largest bead and follows a linear evolution with regards to the squared acoustic amplitude, which is consistent with the radiation force theoretical model. The experimental uncertainty on the stiffness is about 22% on average.

The experimental results are then compared to the 3D model for the radiation force. For this purpose, the incident acoustic field is measured and its beam shape coefficients are determined, then allowing the acoustic force estimation from the experimental field. The direct comparison displays a significant discrepancy which can be resolved using one single amplitude coefficient applied to the model. This coefficient includes several effects like the acoustic measurement uncertainty, the modulation of the acoustic field allowing the neutralization of the rotation induced by the vortex beam, the residual varying gravity and the acoustic streaming. Finally, the application of the correction factor results in very good agreement between experimental and theoretical data, with relative errors of 8.4% on average. Thus, calibration of the axial stiffness of the acoustic tweezers can be realized experimentally in microgravity or theoretically if the acoustic pressure field is known.

This study opens the way towards the use of acoustic tweezers as a scientific tool capable of applying calibrated forces in different field of interest, like scientific research in microgravity, but also on the ground, for microrobotics or biomedical applications on condition that the device is rescaled for the intented purposes.

Acknowledgements

We acknowledge funding from CNES through the GDR MFA Action ID 5878, 6265 and 7330. We thank Novespace for their continuous help in preparing the parabolic flights. We also wish to thank J.M. Citerne for conceiving the setup adapted to the Airbus Zero-G constraints, H. Moingeon for the electronic developments, and C. Ollivon for his precious help in the fabrication of the ultrasonic tweezers.

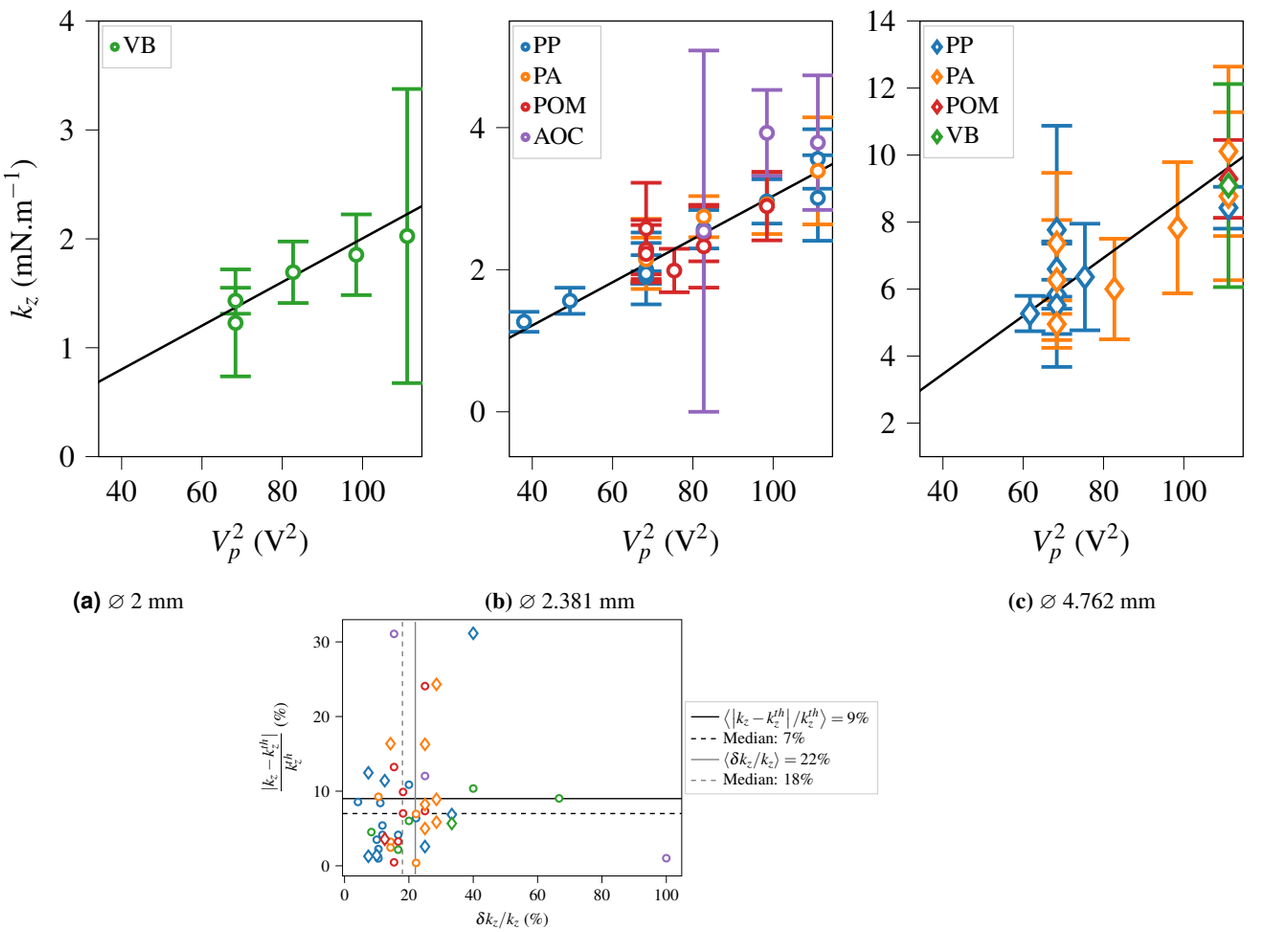

Figure 9. (a)-(c) Comparison of experimental (points with errorbars) and corrected theoretical (black solid lines) stiffnesses (cf. Equation 8) for various beads as a function of the acoustic emission voltage. The theoretical stiffness is determined by the slope of the axial radiation force, calculated around the point of abscissa z corresponding to $F_z = 0$. (d) Differences between theoretical and experimental stiffnesses (cf. Equation 10) as a function of the uncertainty on the experimental stiffness (cf. Equation 11). The averages (solid lines) and medians (dashed lines) of the deviations between experimental and theoretical data (horizontal line), as well as the experimental uncertainty of the stiffness (vertical line) are also shown.

Author contributions statement

All authors conceived and conducted the experiments. All authors analyzed the results. All authors reviewed the manuscript.

Data Availability

The data that support the findings of this study are available from the corresponding author upon reasonable request.

References

1. Ashkin, A., Dziedzic, J. M., Bjorkholm, J. E. & Chu, S. Observation of a single-beam gradient force optical trap for dielectric particles. *Opt. Lett.* **11**, 288 (1986). DOI 10.1364/OL.11.000288.
2. Marzo, A. *et al.* Holographic acoustic elements for manipulation of levitated objects. *Nat. Commun.* **6**, 8661 (2015). DOI 10.1038/ncomms9661.
3. Marzo, A., Caleap, M. & Drinkwater, B. W. Acoustic Virtual Vortices with Tunable Orbital Angular Momentum for Trapping of Mie Particles. *Phys. Rev. Lett.* 6 (2018).
4. Baresch, D., Thomas, J.-L. & Marchiano, R. Observation of a Single-Beam Gradient Force Acoustical Trap for Elastic Particles: Acoustical Tweezers. *Phys. Rev. Lett.* **116**, 024301 (2016). DOI 10.1103/PhysRevLett.116.024301.
5. Shi, J. *et al.* Acoustic tweezers: Patterning cells and microparticles using standing surface acoustic waves (SSAW). *Lab on a Chip* **9**, 2890–2895 (2009). DOI 10.1039/B910595F.
6. Trinh, E. H. Compact acoustic levitation device for studies in fluid dynamics and material science in the laboratory and microgravity. *Rev. Sci. Instruments* **56**, 2059–2065 (1985). DOI 10.1063/1.1138419.
7. Gao, J., Cao, C. & Wei, B. Containerless processing of materials by acoustic levitation. *Adv. Space Res.* **24**, 1293–1297 (1999). DOI 10.1016/S0273-1177(99)00736-X.
8. Santesson, S. & Nilsson, S. Airborne chemistry: Acoustic levitation in chemical analysis. *Anal. Bioanal. Chem.* **378**, 1704–1709 (2004). DOI 10.1007/s00216-003-2403-2.
9. Marston, P. L. & Thiessen, D. B. Manipulation of fluid objects with acoustic radiation pressure. *Annals New York Acad. Sci.* **1027**, 414–434 (2004).
10. Hasegawa, K., Watanabe, A. & Abe, Y. Acoustic Manipulation of Droplets under Reduced Gravity. *Sci. Reports* **9**, 16603 (2019). DOI 10.1038/s41598-019-53281-4.
11. Regnault, G., Mauger, C., Blanc-Benon, P. & Inserra, C. Secondary radiation force between two closely spaced acoustic bubbles. *Phys. Rev. E* **102**, 031101 (2020). DOI 10.1103/PhysRevE.102.031101.
12. Cleve, S., Guédra, M., Mauger, C., Inserra, C. & Blanc-Benon, P. Microstreaming induced by acoustically trapped, non-spherically oscillating microbubbles. *J. Fluid Mech.* **875**, 597–621 (2019). DOI 10.1017/jfm.2019.511.
13. Zhang, P., Bachman, H., Ozcelik, A. & Huang, T. J. Acoustic Microfluidics. *Annu. Rev. Anal. Chem.* **13**, 17–43 (2020). DOI 10.1146/annurev-anchem-090919-102205.
14. Li, M., Xi, N., Wang, Y. & Liu, L. Progress in Nanorobotics for Advancing Biomedicine. *IEEE Transactions on Biomed. Eng.* **68**, 130–147 (2021). DOI 10.1109/TBME.2020.2990380.
15. Hefner, B. T. & Marston, P. L. An acoustical helicoidal wave transducer with applications for the alignment of ultrasonic and underwater systems. *The J. Acoust. Soc. Am.* **106**, 3313–3316 (1999). DOI 10.1121/1.428184.
16. Marchiano, R. & Thomas, J.-L. Synthesis and analysis of linear and nonlinear acoustical vortices. *Phys. Rev. E* **71**, 066616 (2005). DOI 10.1103/PhysRevE.71.066616.
17. Marston, P. L. Radiation force of a helicoidal Bessel beam on a sphere. *The J. Acoust. Soc. Am.* **125**, 3539–3547 (2009). DOI 10.1121/1.3119625.
18. Zhang, L. & Marston, P. L. Geometrical interpretation of negative radiation forces of acoustical Bessel beams on spheres. *Phys. Rev. E* **84**, 035601 (2011). DOI 10.1103/PhysRevE.84.035601.
19. Baresch, D. & Garbin, V. Acoustic trapping of microbubbles in complex environments and controlled payload release. *Proc. Natl. Acad. Sci.* **117**, 15490–15496 (2020). DOI 10.1073/pnas.2003569117.
20. Nikolaeva, A. V., Tsysar, S. A. & Sapozhnikov, O. A. Measuring the radiation force of megahertz ultrasound acting on a solid spherical scatterer. *Acoust. Phys.* **62**, 38–45 (2016). DOI 10.1134/S1063771016010048.

21. Ghanem, M. A., Maxwell, A. D., Sapozhnikov, O. A., Khokhlova, V. A. & Bailey, M. R. Quantification of Acoustic Radiation Forces on Solid Objects in Fluid. *Phys. Rev. Appl.* **12**, 044076 (2019). DOI 10.1103/PhysRevApplied.12.044076.

22. Baresch, D., Thomas, J.-L. & Marchiano, R. Spherical vortex beams of high radial degree for enhanced single-beam tweezers. *J. Appl. Phys.* **113**, 184901 (2013). DOI 10.1063/1.4803078.

23. Sapozhnikov, O. A. & Bailey, M. R. Radiation force of an arbitrary acoustic beam on an elastic sphere in a fluid. *The J. Acoust. Soc. Am.* **133**, 661–676 (2013). DOI 10.1121/1.4773924.

24. Whymark, R. Acoustic field positioning for containerless processing. *Ultrason.* **13**, 251–261 (1975). DOI 10.1016/0041-624X(75)90072-4.

25. Xie, W. J., Cao, C. D., Lü, Y. J. & Wei, B. Levitation of Iridium and Liquid Mercury by Ultrasound. *Phys. Rev. Lett.* **89**, 104304 (2002). DOI 10.1103/PhysRevLett.89.104304.

26. Weber, J. K. R., Rey, C. A., Neuefeind, J. & Benmore, C. J. Acoustic levitator for structure measurements on low temperature liquid droplets. *Rev. Sci. Instruments* **80**, 083904 (2009). DOI 10.1063/1.3196177.

27. Rey, C. A., Merkley, D. R., Hammarlund, G. R. & Danley, T. J. Acoustic levitation technique for containerless processing at high temperatures in space. *Metall. Transactions A* **19**, 2619–2623 (1988). DOI 10.1007/BF02645792.

28. Wang, T. G., Anilkumar, A. V., Lee, C. P. & Lin, K. C. Bifurcation of rotating liquid drops: Results from USML-1 experiments in Space. *J. Fluid Mech.* **276**, 389–403 (1994). DOI 10.1017/S0022112094002612.

29. Wang, T. G., Anilkumar, A. V. & Lee, C. P. Oscillations of liquid drops: Results from USML-1 experiments in Space. *J. Fluid Mech.* **308**, 1–14 (1996). DOI 10.1017/S002211209600136X.

30. Trinh, E. H. & Hsu, C. J. Acoustic levitation methods for density measurements. *The J. Acoust. Soc. Am.* **80**, 1757–1761 (1986). DOI 10.1121/1.394290.

31. Zhao, D., Thomas, J.-L. & Marchiano, R. Computation of the radiation force exerted by the acoustic tweezers using pressure field measurements. *The J. Acoust. Soc. Am.* **146**, 1650–1660 (2019). DOI 10.1121/1.5126095.

32. Zhang, L. & Marston, P. L. Angular momentum flux of nonparaxial acoustic vortex beams and torques on axisymmetric objects. *Phys. Rev. E* **84**, 065601 (2011). DOI 10.1103/PhysRevE.84.065601.

33. Baresch, D., Thomas, J.-L. & Marchiano, R. Orbital Angular Momentum Transfer to Stably Trapped Elastic Particles in Acoustical Vortex Beams. *Phys. Rev. Lett.* **121**, 074301 (2018). DOI 10.1103/PhysRevLett.121.074301.

34. Lamprecht, A., Schwarz, T., Wang, J. & Dual, J. Viscous torque on spherical micro particles in two orthogonal acoustic standing wave fields. *The J. Acoust. Soc. Am.* **138**, 23–32 (2015). DOI 10.1121/1.4922175.

35. Baresch, D., Thomas, J.-L. & Marchiano, R. Three-dimensional acoustic radiation force on an arbitrarily located elastic sphere. *The J. Acoust. Soc. Am.* **133**, 25–36 (2013). DOI 10.1121/1.4770256.

36. Eckart, C. Vortices and Streams Caused by Sound Waves. *Phys. Rev.* **73**, 68–76 (1948). DOI 10.1103/PhysRev.73.68.

37. Nyborg, W. L. Acoustic Streaming due to Attenuated Plane Waves. *The J. Acoust. Soc. Am.* **25**, 68–75 (1953). DOI 10.1121/1.1907010.

38. Lighthill, S. J. Acoustic streaming. *J. Sound Vib.* **61**, 391–418 (1978). DOI 10.1016/0022-460X(78)90388-7.

39. Baudoin, M. & Thomas, J.-L. Acoustic Tweezers for Particle and Fluid Micromanipulation. *Annu. Rev. Fluid Mech.* **52**, 205–234 (2020). DOI 10.1146/annurev-fluid-010719-060154.

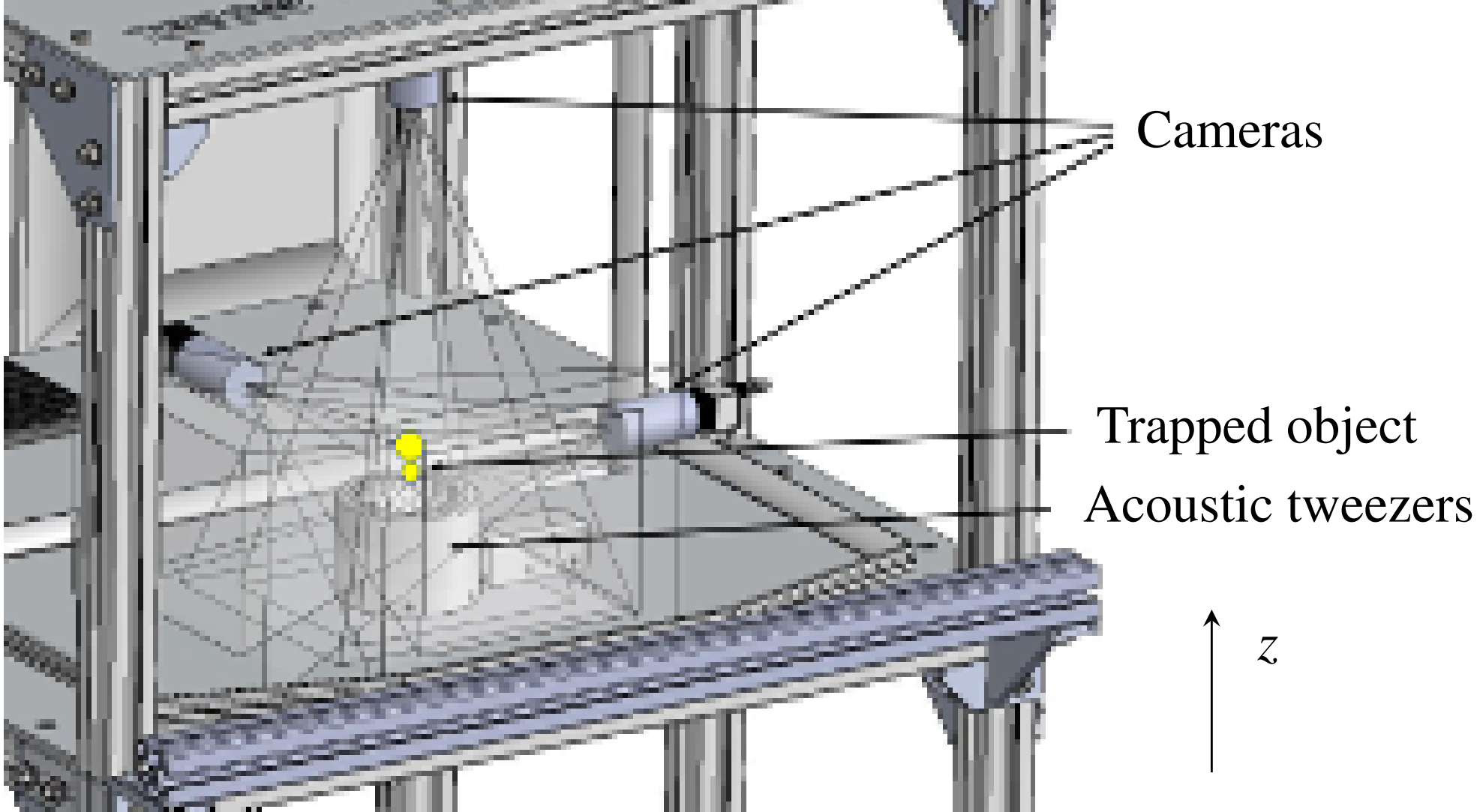
Cameras
Trapped object
Acoustic tweezers
z

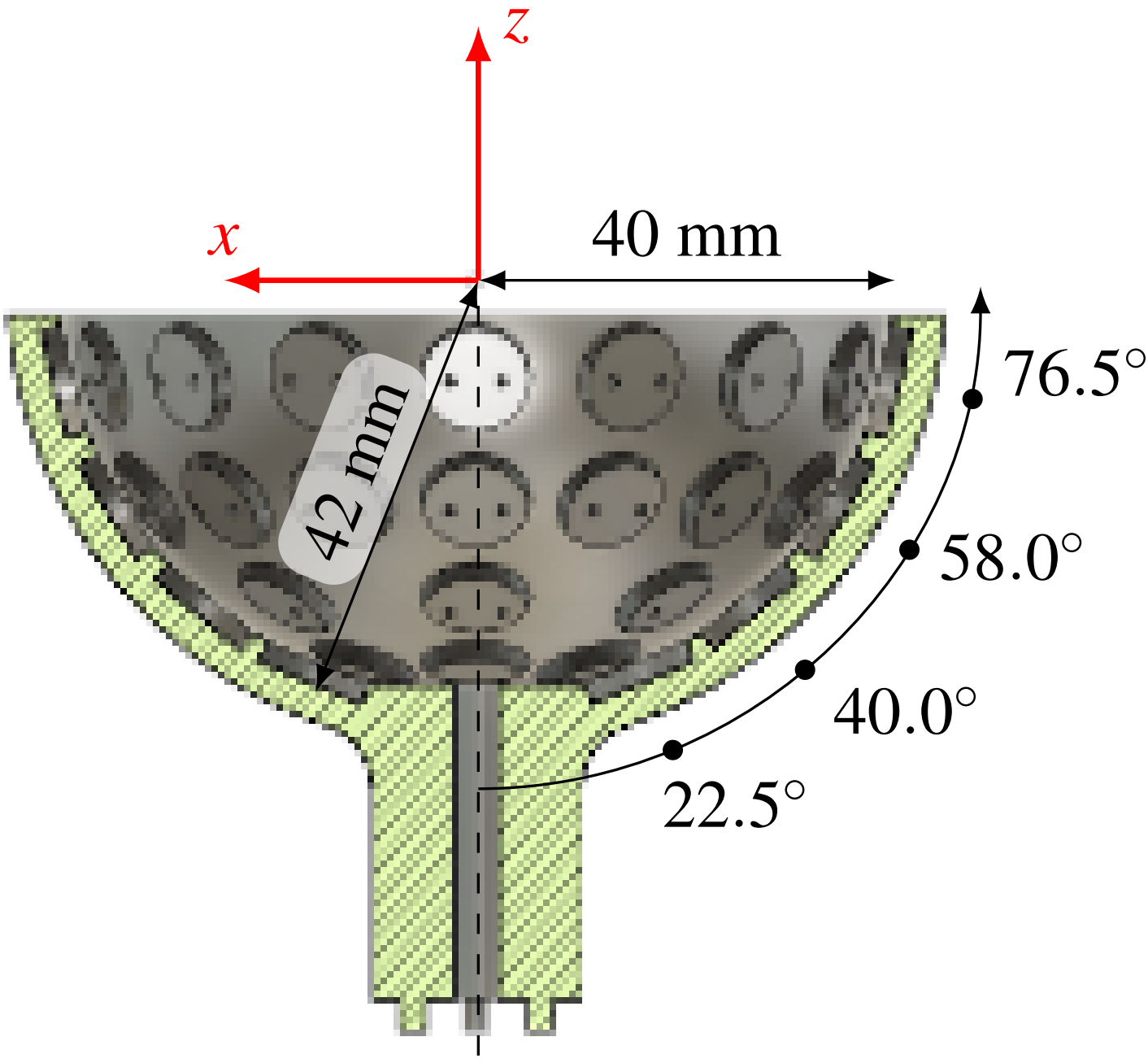
z
x
40 mm
42 mm
76.5°
58.0°
40.0°
22.5°

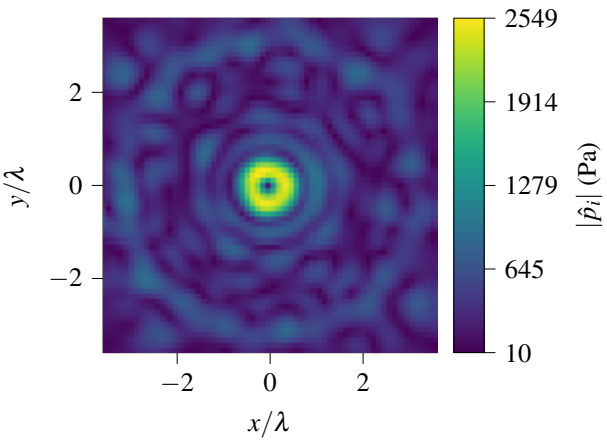
2549
1914
1279
645
10
$|\hat{p}_i|$ (Pa)
2
0
−2
y/λ
−2
0
2
x/λ

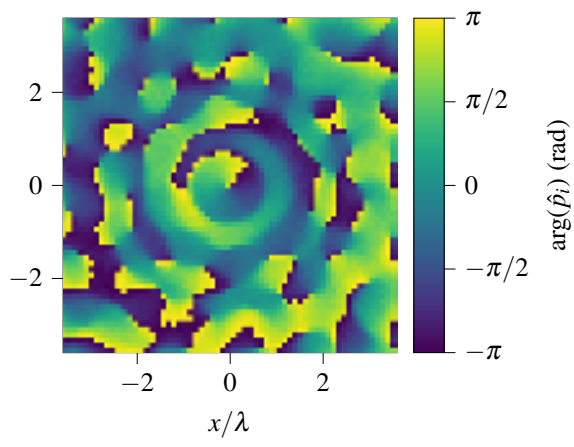
π
$\pi/2$
0
$-\pi/2$
$-\pi$
$\arg(\hat{p}_i)$ (rad)
2
0
−2
−2
0
2
x/λ

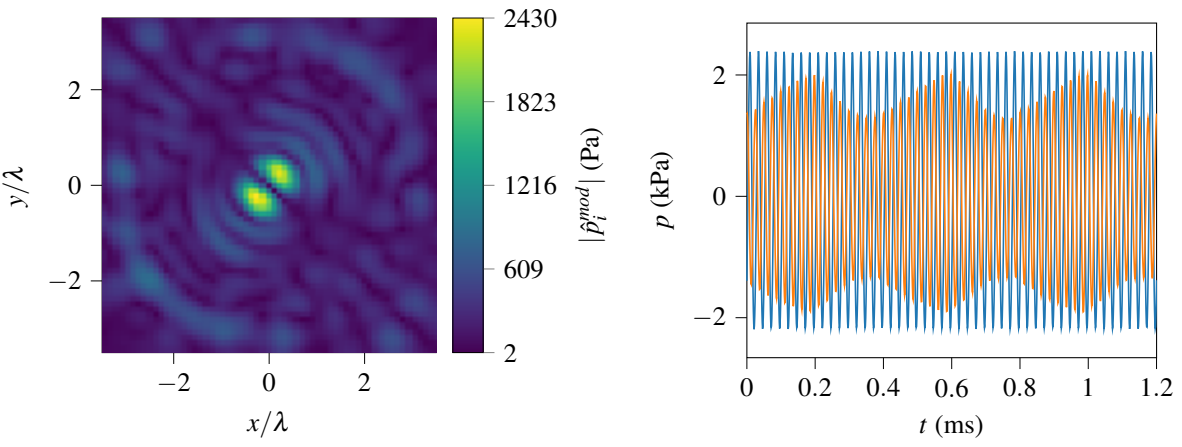
2
0
−2
y/λ
−2
0
2
x/λ
2430
1823
1216
609
2
$|\hat{p}_i^{mod}|$ (Pa)
2
0
−2
p (kPa)
0
0.2
0.4
0.6
0.8
1
1.2
t (ms)

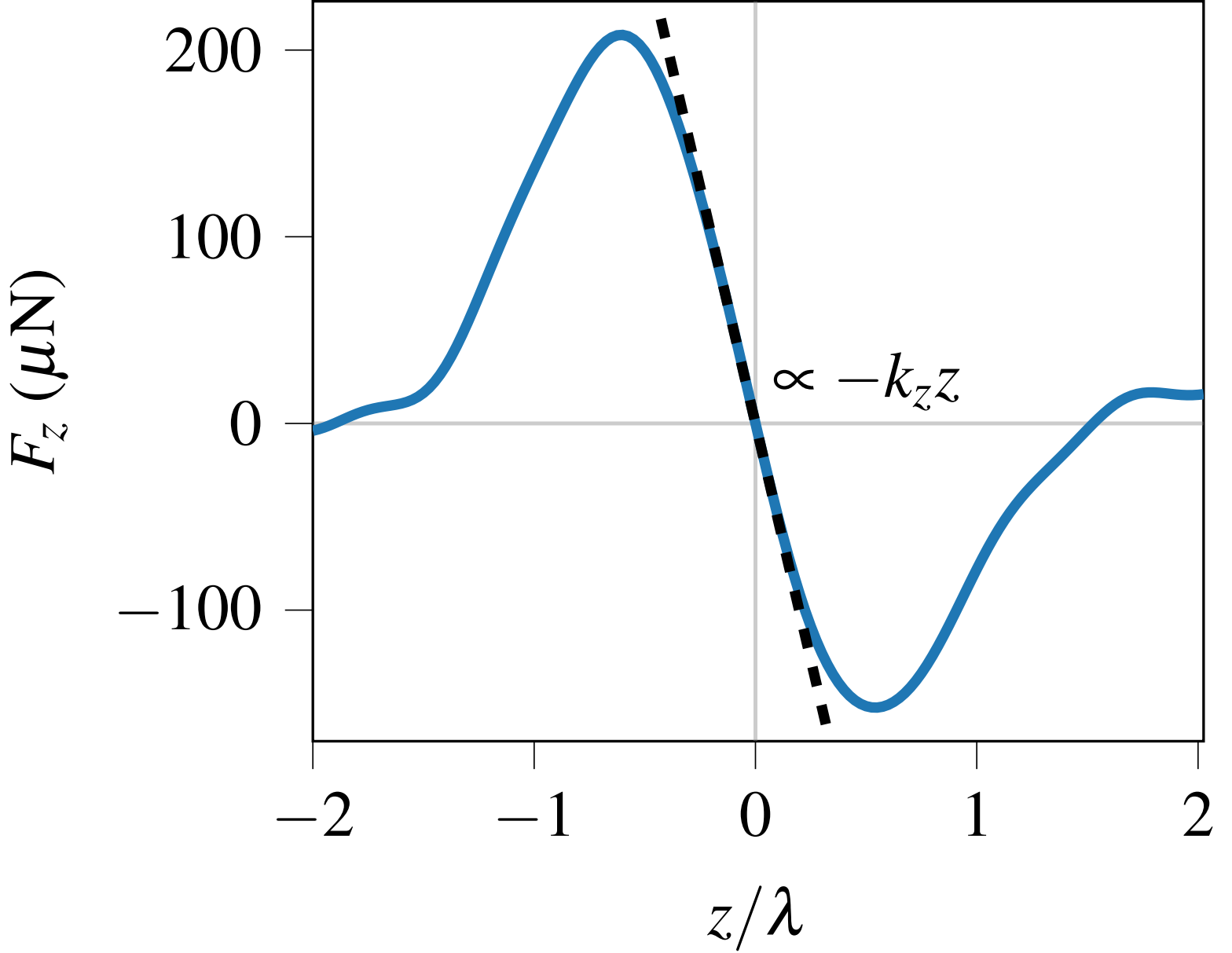
200
100
0
−100
F_z (μN)
$\propto -k_z z$
−2
−1
0
1
2
z/λ

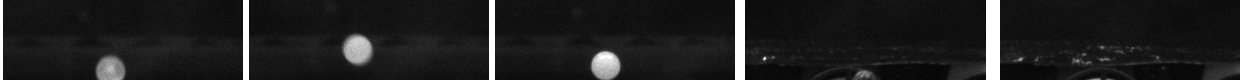

∅2.381 mm PP ∅2.381 mm PA ∅2.381 mm POM ∅2 mm BG ∅2.381 mm AOC

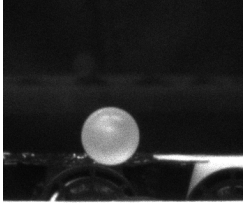

∅4.762 mm PP

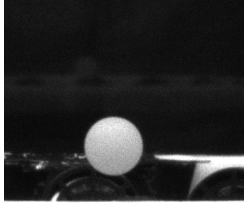

∅4.762 mm PA

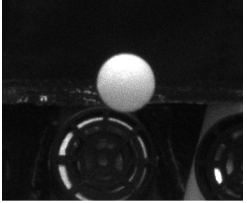

∅4.762 mm POM

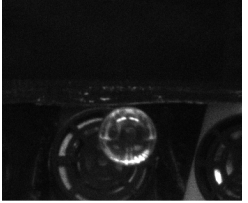

∅4.762 mm BG

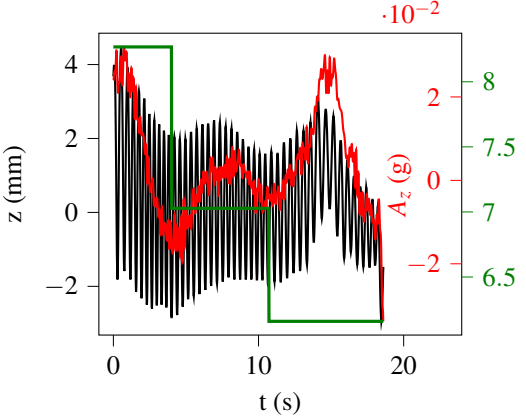
·10−2
4
2
0
−2
z (mm)
2
0
−2
A_z (g)
8
7.5
7
6.5
V_p (V)
0
10
20
t (s)

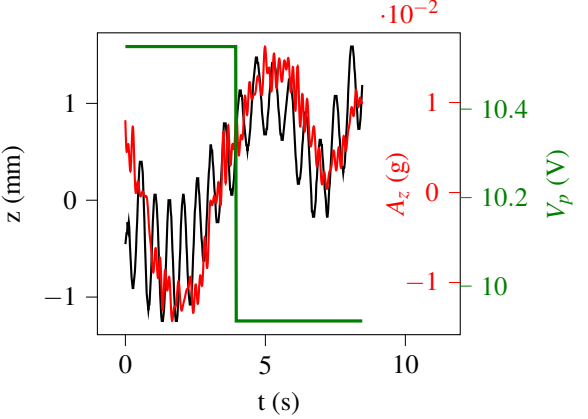
·10−2
1
0
−1
z (mm)
1
0
−1
A_z (g)
10.4
10.2
10
V_p (V)
0
5
10
t (s)

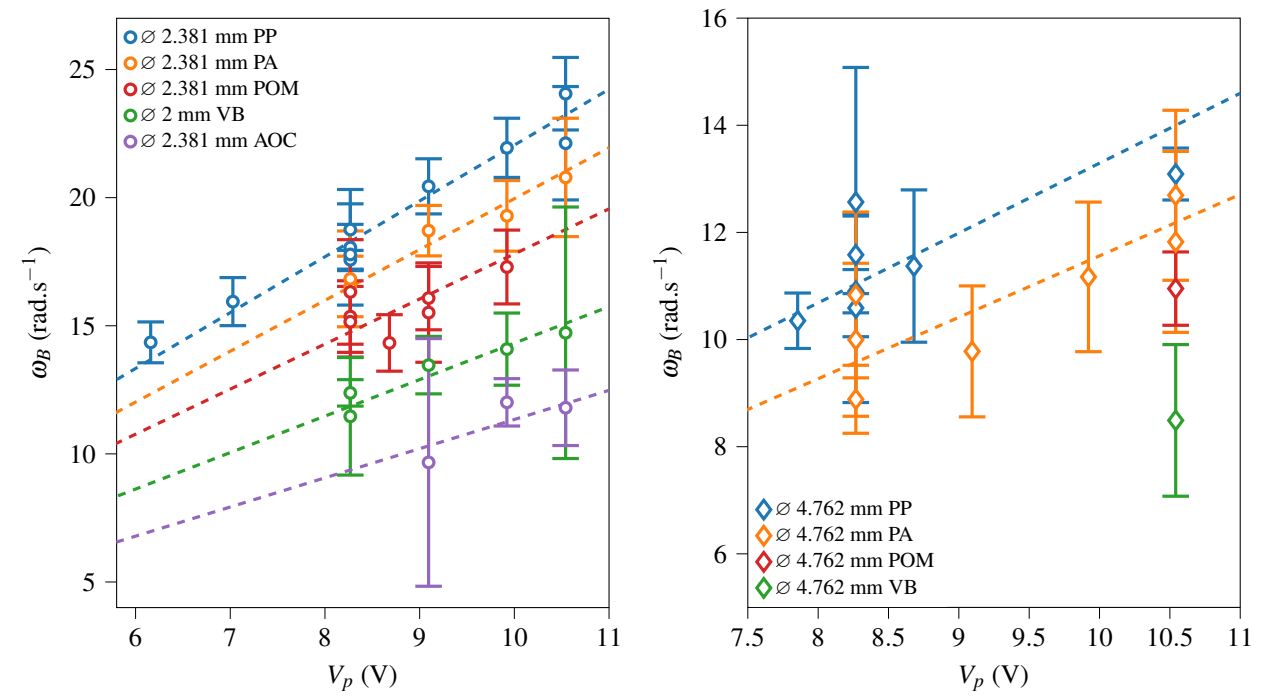
⌀ 2.381 mm PP
⌀ 2.381 mm PA
⌀ 2.381 mm POM
⌀ 2 mm VB
⌀ 2.381 mm AOC
ω_B (rad.s^{-1})
V_p (V)
⌀ 4.762 mm PP
⌀ 4.762 mm PA
⌀ 4.762 mm POM
⌀ 4.762 mm VB
ω_B (rad.s^{-1})
V_p (V)

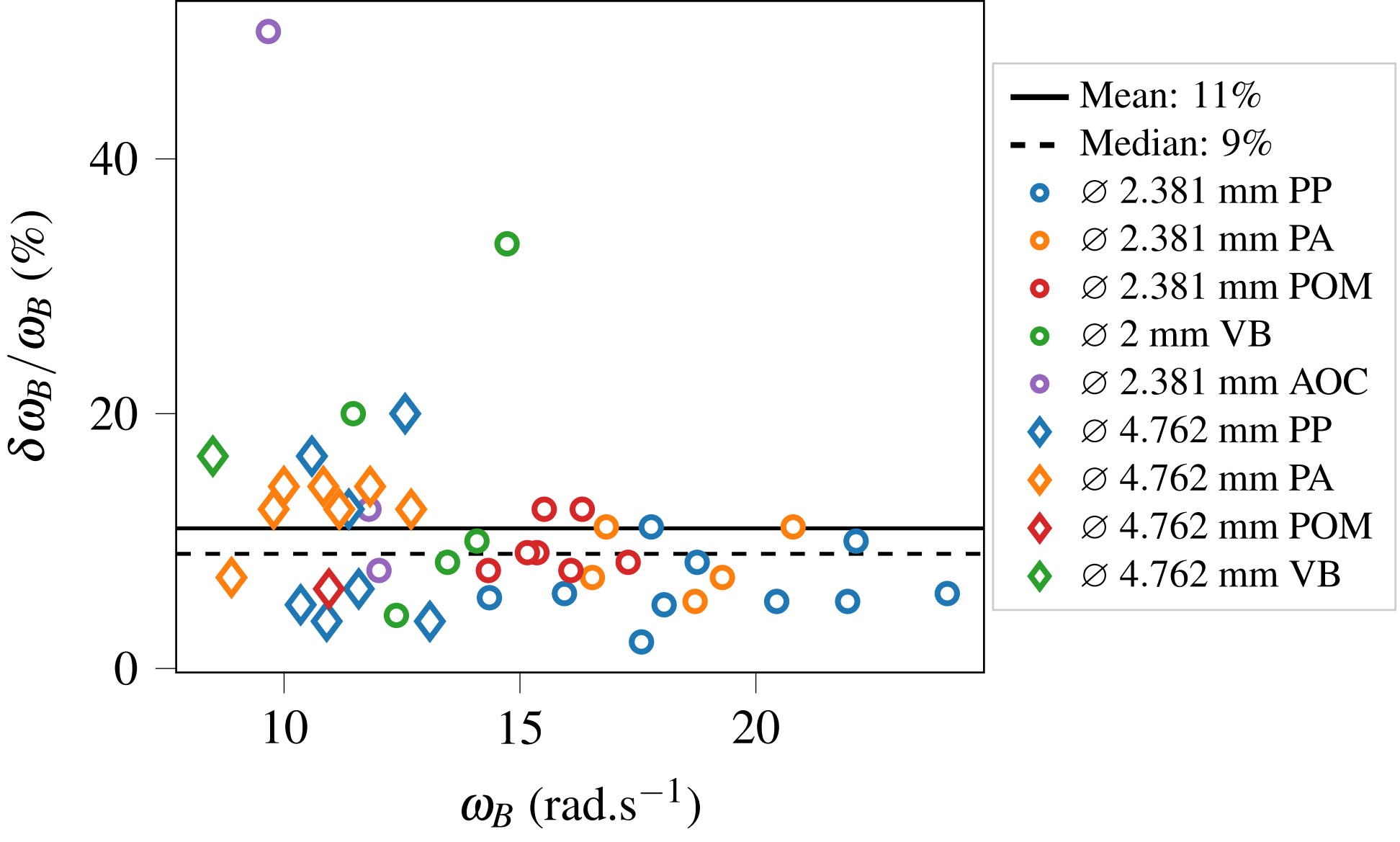
40
20
0
10
15
20
$\delta\omega_B/\omega_B$ (%)
ω_B (rad.s^{-1})
Mean: 11%
Median: 9%
∅ 2.381 mm PP
∅ 2.381 mm PA
∅ 2.381 mm POM
∅ 2 mm VB
∅ 2.381 mm AOC
∅ 4.762 mm PP
∅ 4.762 mm PA
∅ 4.762 mm POM
∅ 4.762 mm VB

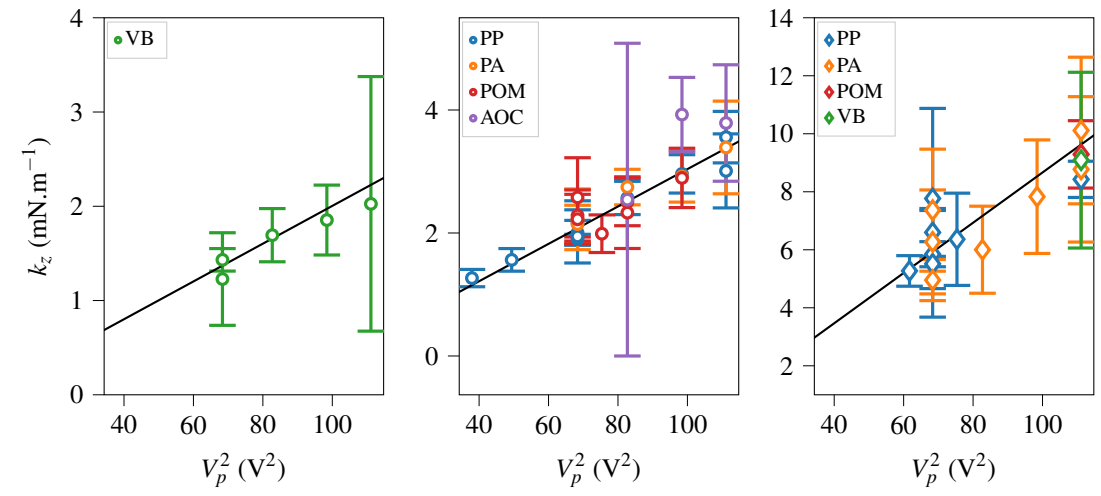
VB
PP
PA
POM
AOC
k_z (mN.m^{-1})
V_p^2 (V^2)
V_p^2 (V^2)
V_p^2 (V^2)

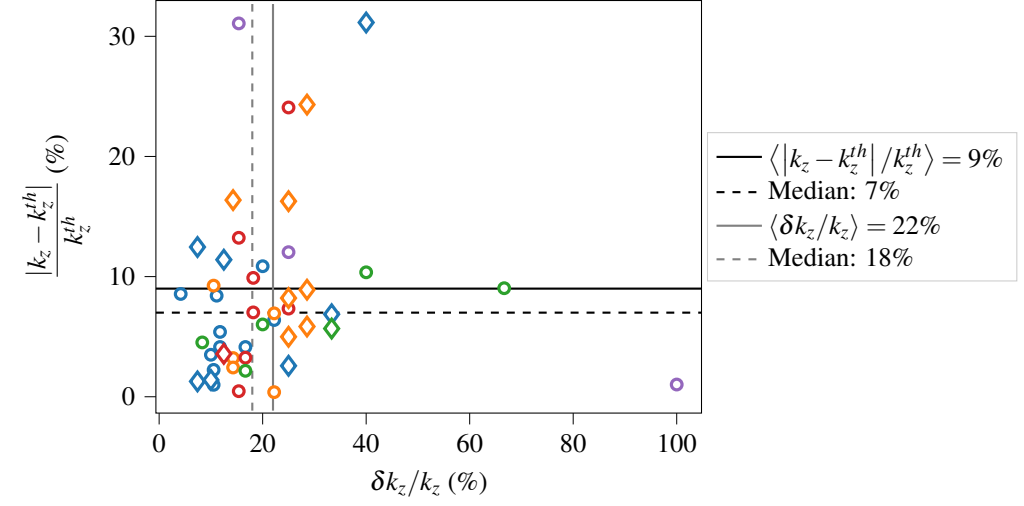
30
20
10
0
0
20
40
60
80
100
$\frac{|k_z - k_z^{th}|}{k_z^{th}}$ (%)
$\delta k_z/k_z$ (%)
$\langle |k_z - k_z^{th}| / k_z^{th} \rangle = 9\%$
Median: 7%
$\langle \delta k_z/k_z \rangle = 22\%$
Median: 18%